Nanoscale

Accepted Manuscript

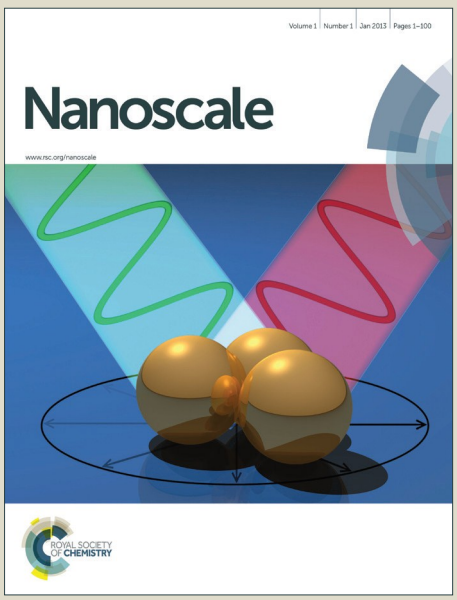

ROYAL SOCIETY OF CHEMISTRY

www.rsc.org/nanoscale

Improved Electrochemical Performance of Spinel $LiMn_{1.5}Ni_{0.5}O_4$ through MgF_2 Nano-coating

Qing Wu, [†] [a] Xiaoping Zhang, [†] [a] Shuwei Sun,[a] Ning Wan,[a] Du Pan,[a]

Ying Bai*[a] [b], Huiyuan Zhu[b], Yong-Sheng Hu[c], Sheng Dai[b]

[a] Key Laboratory of Photovoltaic Materials of Henan Province and School of Physics & Electronics, Henan University, Kaifeng 475004, PR China.

[b] Chemical Sciences Division, Oak Ridge National Laboratory, Oak Ridge, TN 37831, USA.

[c] Institute of Physics, Chinese Academy of Sciences, Beijing 100190, PR China.

Abstract: Spinel $LiMn_{1.5}Ni_{0.5}O_4$ (LMNO) cathode material synthesized by a sol-gel method is modified by MgF_2 nano-coating via wet coating strategy. The results of X-ray diffraction (XRD), Raman spectroscopy, field emission scanning electron microscopy (FESEM) and high resolution transmission electron microscopy (HRTEM) showed that the MgF_2 nano-coating layers do not physically change the bulk structure of pristine material. Compared with the pristine compound, the MgF_2-coated LMNO electrodes display enhanced cycling stabilities. Particularly, the 5 wt.% MgF_2-coated LMNO demonstrates the best reversibility, with capacity retention of 89.9% after 100 cycles, much higher than that of the pristine material, 69.3%. The dQ/dV analysis and apparent Li^+ diffusion coefficient calculation prove that the kinetic property is enhanced after MgF_2 surface modification, which partly explains the improved electrochemical performances. Electrochemical impedance spectroscopy (EIS) and flourier transform infrared spectroscopy (FTIR) data confirm that MgF_2 coating layer helps in suppressing the fast growth of solid electrolyte interface (SEI) film in repeated cycling, which effectively stabilizes the spinel structure. Additionally, differential

scanning calorimetry (DSC) tests show that the MgF_2 nano-coating layer also helps in enhancing the thermal stability of LMNO cathode.

Keywords: Spinel $LiMn_{1.5}Ni_{0.5}O_4$ · Nano-coating · Cycling performance · Solid electrolyte interface (SEI) film· Lithium-ion batteries (LIBs)

† These authors contributed equally to this work.

***Corresponding author.**

E-mail addresses: ybai@henu.edu.cn (Ying Bai).

Introduction

Lithium-ion batteries (LIBs) have already been ubiquitous in our daily life and served not only in the large-scale energy storage but also in consumer electronics.[1] In recent years, the increasing demand for high-energy and high-power LIBs in the development of hybrid electric vehicles (HEVs) and electric vehicles (EVs) has stimulated great research interest in advanced electrode materials.[2-6] As a promising high energy density cathode material for LIBs, spinel-structured $LiMn_{1.5}Ni_{0.5}O_4$ (LMNO) attracts great attention, due to its higher working voltage (4.7 V) than commercialized cathodes such as $LiFePO_4$ (3.4 V), $LiCoO_2$ (3.9 V) and $LiMn_2O_4$ (4.1 V).[7,8]

However, this material still has some drawbacks, such as capacity fading during cycling derived from the decomposition of electrolyte and the dissolution of Mn element at high voltage.[9,10] One approach to improve the electrochemical performance of a cathode material is to modify the cathode surface with materials inert against the electrolyte, especially HF. In an attempt to overcome these problems, coating the surface of pristine powder with stable materials has been widely investigated. According to some previous studies, metal oxides and metal phosphate are

commonly used as coating materials.[11-21] Nevertheless, it was reported that metal oxides and metal phosphates can be converted into the corresponding metal fluorides through the exposure to trace of HF in electrochemical environment.[17-19] For instance, Myung et al. reported that a metal-oxide coating layer on $Li_{1.05}Ni_{0.4}Co_{0.15}Mn_{0.4}O_2$ acted as an HF scavenger, and they suggested the following reaction: $Al_2O_3+6HF\rightarrow 2AlF_3+3H_2O$.[20,21] Bai et al. reported that the conversion of YPO_4 to YF_3 even happened in chemical storage of YPO_4 coated $LiCoO_2$.[17] Moreover, Liu et al. indicated that AlF_3 is one of the components of SEI film formed on the surface of $LiCoO_2$ immersed in the electrolyte containing Al_2O_3 additive.[19] Enlightened by the previous studies, metal fluorides are most likely the ultimate products making substantial contribution in repeated electrochemical cycling.

MgF_2 is widely applied in the design and development of various optical thin films and multilayer photonic crystals for its properties including high hardness, good thermal stability, low refractive index, higher transmissivity in the ultraviolet, visible and infrared range, low absorption and wide band gap.[22] Cho et al. coated MgF_2 on the surface of $LiCoO_2$ and effectively improved the electrochemical performances.[23] Besides, Lee et al. coated MgF_2 on the surface of $LiCoO_2$ and $Li[Li_{0.2}Ni_{0.2}Mn_{0.6}]O_2$, which also effectively suppressed the capacity fading.[24,25]

In this study, LMNO was coated with different contents of MgF_2 through a simple replacement reaction, which is workable and repeatable in practical applications. Comparatively, the 5 wt.% MgF_2 coated LMNO electrode exhibits the optimal cycling stability. Further, the mechanism for the improvements has also been intensively explored. Besides, it is found that the thermal stability of LMNO electrode has been improved by MgF_2 surface modification.

Experimental

Sample preparation

Pristine LMNO was synthesized by a sol-gel method as described in Ref.[26] All the chemical reagents used in this work was of analytical grade. In a typical experiment, certain amounts of lithium acetate, manganese acetate, nickel acetate and citric acid were dissolved separately into distilled water. The molar ratio of Li:Mn:Ni = 1.05:1.5:0.5 and the mole ratio between the total transition metal ions and citric acid was fixed at 1:1.5. After homogeneously dissolved, the transparent manganese acetate solution was mixed with the lithium acetate solution and the nickel acetate solution to form lithium/manganese/nickel solution by continuous stirring. Afterwards, ammonium hydroxide was slowly added into the mixture to adjust the pH value to about 7.0. Then, the mixture was stirred vigorously at 80 ℃ till viscous gel was formed. Afterwards the gel was annealed at 550 °C in air for 6 h to eliminate organic contents. Then the precursors were further annealed in a muffle furnace at 800 °C in air for 10 h and naturally cooled down to room temperature, finally yielding black powder of LMNO.

To prepare MgF_2-coated LMNO, magnesium nitrate nonahydrate and ammonium fluoride were separately dissolved in distilled water. After that, the as-prepared LMNO powders were dispersed in the magnesium nitrate nonahydrate solution. Then, ammonium fluoride was added in drop by drop. The molar ratio of the Mg source to the F source was adjusted to be 1:2 and the amount of MgF_2 in the solution varied from 3 wt.%, 5 wt.% and 7 wt.%. After repeated rinsing and filtering, the precipitations were heated at 400 °C for 5 h in air to obtain the MgF_2-coated LMNO samples. For comparison, the as-prepared bare sample was also post-annealed in the same condition (400 ℃ for 5 h in the air) and was thus defined and used as pristine material in the

following experiment and analysis.

Physical characterizations

The surface morphologies of the samples were observed through field emission scanning electron microscopy (FESEM, JEOL JSM-7001F), operated at 15 kV. Energy Dispersive Spectrometer (EDS) was applied to determine the elements of powders together with SEM in a large field of view. EDS were collected by a APOLLO X silicon drift X-ray detector under at an acceleration voltage of 15 kV. The image of high resolution transmission electron microscopy (HRTEM) was collected on JEOL JEM 2010 equipment to investigate the microstructure of samples. The inductively coupled plasma (ICP) analysis was performed on Thermo Fisher ICAP 6300 to determine the exact chemical compositions of the samples. The X-ray diffraction (XRD) patterns of the as-prepared LMNO samples were measured on Bruker D8 Advance diffractometer (Bruker, Germany) with the slit size of 0.6 mm and Cu Kα radiation of $\lambda \sim 0.15418$ nm between 10° and 80° at a scan rate of 0.04° s^{-1}. In addition, the structural parameters were refined by the Rietveld method from XRD data with a 2 theta range from 10° to 80° using the Fullproof software. Fourier transform infrared (FTIR) spectra were performed on a pellet made of active materials and KBr powder by using an AVATAR360 Fourier-transformed infrared spectrometer over the range 400-4000 cm^{-1} to determine the composition of samples after 5 cycles in charged state. The Raman spectra were collected on a laser Raman Spectrometer (RM-1000, Renishaw) with 632.8 nm He-Ne laser. X-ray photoelectron spectroscopy (XPS) was performed on a Thermo Electron Corporation spectrometer with an Al Ka (1486.6 eV) radiation.

Electrochemical characteristics

The working electrodes were prepared by casting a slurry of 80 wt.% active material (0, 3, 5

and 7 wt.% MgF_2-coated LMNO), 10 wt.% carbon black and 10 wt.% PVDF (polyvinylidene fluoride) on Al foil. Afterwards, the electrode sheets were dried at 120 °C for 12 h under vacuum, and cut into squares with area of 0.64 cm^2. A Li foil and Celgard 2400 were used as counter electrode and separator, respectively. The electrolyte consists of 1 M $LiPF_6$ dissolved in a mixture of ethylene carbonate (EC) and dimethyl carbonate (DMC) (1:1 by volume). Batteries were fabricated in an argon filled glove-box with H_2O and O_2 contents less than 1 ppm. Before electrochemical tests, the batteries were aged for 24 h to ensure sufficient soakage. Cycling performances were evaluated by a Neware battery tester (CT-3008W-5V3A-S4) between 3.5 and 4.9 V. The electrochemical impedance spectroscopy (EIS) investigations were performed on an electrochemical workstation with three electrode systems (CHI660C, Shanghai Chenhua). After 10, 20, 50, 80 and 100 cycles at a current density of 0.1 C, the cells were charged and aged for two days to reach equilibrium at 4.9 V before the EIS spectra were measured. The EIS measurements were performed at different cycles with AC amplitude of 10 mV over a frequency range from 100 kHz to 5 mHz. The interface exothermic reaction between the charged LMNO and the electrolyte was examined by differential scanning calorimetry (DSC, TA Q600) measurements, where the cells were charged to 4.9 V at a current density of 0.1 C and then disassemble in an argon-filled glove-box with the content H_2O and O_2 less than 1 ppm to remove the charged cathode. After clean up, the cathode was hermetically sealed in a high-pressure Al pan. The DSC measurements were performed in a temperature range from room temperature to 350 °C at a rate of 5 °C min^{-1} under a dry Ar atmosphere. To ensure the accuracy of the experiment, each type of experiment was tested no less than 5 times for each sample. Although occasionally, a small amount of cells will die at high voltages in cycling, the conformance of the test results is good.

Results and discussion

Physical characteristics

The results of Rietveld refinement X-ray diffraction patterns of pristine and MgF_2-coated LMNO are shown in Fig. 1. All the diffraction peaks agree well with those in JCPDS card 80-2162, assigning to $Fd\bar{3}m$ space group of the disordered framework. The strong and sharp diffraction peaks indicate that the as-obtained pristine and MgF_2-coated LMNO materials are well-crystallized. No diffraction peak from MgF_2 can be detected in the XRD patterns, which could be attributed to its low content. The lattice parameters and grain sizes obtained through Rietveld refinement, as shown in Table 1. It is known that under certain circumstances the series of high voltage spinel LMNO can exhibit 3/1 transition metal ordering on the 4b and 12d octahedral sites of space group $P4_332$ versus random octahedral 16 sites of $Fd\bar{3}m$. The LMNO spinel structure can be ordered ($P4_332$) or disordered ($Fd\bar{3}m$) framework.[27] As can be seen in Table 1, the lattice parameters decreased after coating MgF_2 layer. Since the radius of Mn^{3+} is larger than that of Mn^{4+}, thus, this change indicates that the MgF_2 coating layer induces a disorder-order phase transition, which corresponds to a small fraction of the $Fd\bar{3}m$ phase converting to the $P4_332$ phase. This transition will reduce the amount of Mn^{3+} in spinel, thereby improving the electrochemical performance of LMNO.[28] However, the percentage of ordered phase is low in all of these samples, for the main phase in this framework is $Fd\bar{3}m$, as shown in XRD patterns. Additionally, O vacancies can be observed in all the four samples from the refined result, which consequently, will lead to the existence of Mn^{3+},[29] which will be confirmed by the subsequent dQ/dV result (Fig. 5).

Raman spectra are employed to reveal the subtle surface compositional and structural information of the pristine and MgF_2-coated LMNO, which are presented in Fig. S1 (Supporting

Information). The Raman bands at 632, 588, 491, 399 and 335 cm^{-1} are similar to the reference.[30] The vibration peak at 632 cm^{-1} is assigned to the symmetric Mn–O stretching vibration.[31] Bands at 588 cm^{-1} ($F_{2g}^{(1)}$), 491 cm^{-1} ($F_{2g}^{(2)}$), 399 cm^{-1} (Eg) and 335 cm^{-1} ($F_{2g}^{(3)}$) can be ascribed to the Ni–O stretching mode in the structure.[30] No obvious difference could be observed after surface modification and the detailed fitting of the vibration peaks shows that the peak width and intensity (integrated area) remain almost unchanged with the increase of coating content, even when it reaches 7 wt.%. This indicates that the surface modification does not influence the structure of LMNO, corresponding with the XRD results.

Fig. 2 shows the surface morphologies of LMNO samples and element mapping images of 5 wt.% MgF_2-coated LMNO. It can be seen apparently that the morphologies of the four samples are very similar, demonstrating the characteristic shape of well-crystallized spinel phase. All samples show clean surface and clear boundaries with average particle size of 200 nm. After surface modification with different contents of MgF_2, no obvious difference can be observed from the SEM images, and the particle surface still looks smooth and clean for 3, 5 and 7 wt.% MgF_2-coated samples (Fig. 2b-d), indicating that the coating layer is very thin. Fig. 2e and f display the element mappings of Mg and overlays of Mg and F for the MgF_2-coated spinel powders. As clearly observed in these Fig.s, elements of Mg and F can be clearly detected by EDS collection, indicating that the MgF_2 coating layer deposited outside the LMNO particle surface is homogeneous. ICP analysis was also conducted to determine the exact content of MgF_2 in the coated materials. It shows that the actual contents of MgF_2 are 2.78±0.01, 4.46±0.01 and 6.29±0.01 wt% for 3, 5 and 7 wt.% MgF_2-coated LMNO. Nevertheless, we still name 3, 5 and 7 wt.% MgF_2-coated LMNO hereafter.

To confirm the microstructure of MgF_2 coating layer, TEM was performed on the samples. Fig. 2g-h reveals the TEM images of the pristine and 5 wt.% MgF_2-coated LMNO. As shown in Fig. 2g, a sharp surface without any coating layer can be observed for the pristine LMNO and it shows perfect crystallization. The crystal orientation is viewed along (111), corresponding with the XRD results. On the contrary, the 5 wt.% MgF_2-coated LMNO material (Fig. 2h) exhibits an amorphous and uniform modification layer with thickness of about 2 nm on the surface. In order to confirm the composition of the surface coating layer in Fig. 2h, X-ray photoelectron spectroscopy (XPS) was employed on pristine and 5 wt.% MgF_2-coated LMNO samples. As shown in Fig. S2 (Supporting Information), the signals of Mg 2p and F 1s peaks are clearly observed in the coated sample. The binding energies of Mg 2p (51.2 eV) and F 1s (685.7 eV) agree well with previous literatures.[32-34] This result strongly confirms the surface coating layer of MgF_2. The MgF_2 coating layer outside LMNO particles can avoid the direct contact between the spinel particles and electrolyte and thus improves the interface stability in cycling.

Electrochemical characteristics

The influence of MgF_2 coating layer on the capacity retention of LMNO in the range of 3.5-4.9 V at a current rate of 14.7 mA g^{-1} (0.1 C) is compared in Fig. 3. The pristine LMNO suffers fast capacity fading after 100 cycles, with capacity retention ratio about 69.3%, though it exhibits a higher initial discharge capacity. This poor cycling performance can be presumably ascribed to the vigorous surface reactivity of the Ni^{4+} (from the LMNO) with liquid electrolyte.[35] In comparison, the detailed electrochemical data for the pristine and MgF_2-coated LMNO are listed in Table 2. For MgF_2-coated LMNO electrodes, although their initial discharge capacities monotonically decrease with increasing coating content, they generally demonstrate improved capacity retentions in

repeated cycling. As can be seen in Table 2, MgF_2 surface modification greatly improves the cyclability of LMNO. Favorable cycle stability illustrates good structure stability for the MgF_2-coated LMNO. Comparatively, 5 wt.% MgF_2 coating is the most effective in improving the cycling performance of LMNO. For the 5 wt.% MgF_2-coated LMNO, the capacity retention is 97.3 % after 50 cycles and 89.9% after 100 cycles. The cycling performance gets worse when the MgF_2 content increases from 3 wt.% to 7 wt.%, implying that excessive MgF_2 coating plays a negative role on the surface of LMNO, hindering the lithium ion diffusion and electrons transportation between the LMNO particles and the electrolyte. This will inevitably leads to deterioration of electrochemical performance of the electrode and can be confirmed by Fig. 4.

Fig. 4 displays the galvanostatic cycling profiles of pristine and MgF_2-coated LMNO electrodes between 3.5 and 4.9 V at a current density of 0.1 C. As can be seen from Fig. 4a, two plateaus around 4.0 and 4.7 V are observed, which represent the typical electrochemical behavior of LMNO with $Fd\bar{3}m$ space group.[36] Similarly, the MgF_2-coated LMNO electrode also shows two characteristic plateaus, indicating that the MgF_2 coating does not change the intrinsic structure of LMNO during insertion and extraction of lithium ions. From Fig. 4a, we can learn that charge-discharge curves of pristine LMNO quickly degrade. However, the curves of 3 wt.% and 5 wt.% MgF_2-coated LMNO electrode show good repeatability. Particularly, the 5 wt.% MgF_2-coated electrode exhibits the best cycling retention, indicating that appropriate MgF_2 coating layer helps to maintain the main structure for LMNO. This may be ascribed to the MgF_2 surface modification layer which effectively avoids the direct contact between the electrode and electrolyte, and thus suppresses the side reaction. On the other hand, with the increasing of the content of MgF_2, the coating layer will hinder the transportation of Li^+ ions through the interface between electrode

particles and the electrolyte leading to evident capacity decay, which can be confirmed in Fig. 4d.

In order to explore the mechanism of electrochemical performance improvement of MgF_2 coating layer on LMNO, dQ/dV profiles were collected and presented. Fig. 5 shows the initial dQ/dV profiles for the electrodes fabricated using the pristine and 5 wt.% MgF_2-coated LMNO. The doubles peaks in the 4.6-4.8 V (i.e., reduction) region were assigned to the two-step oxidation of Ni^{2+} to Ni^{3+} and then to Ni^{4+},[36] exhibit no significant difference, indicating that surface coating layer does not change the intrinsic structure of LMNO during insertion and extraction of lithium ions. The redox peaks in the 4 V region are attributed to the Mn^{3+}/Mn^{4+} redox reaction.[8] As can be observed in the inset of Fig. 5, the peak associated with MgF_2-coated LMNO is less intense than that corresponding to the pristine electrode in the 4 V region, indicating the capacity decrease in this voltage region after MgF_2 coating. This phenomenon can be attributed to the increase of the percentage of $P4_332$ phase in the modified electrode, which has higher content of Mn^{4+} and shows cation ordering in the framework, as reported by Hagh et al.[37] It is widely accepted that the difference between redox pairs (D-value) relates to the degree of polarization.[38] Herein, the D-values of pristine and 5 wt.% MgF_2-coated LMNO electrodes are compared in Table 3. It can be observed that the D-values of 5 wt.% MgF_2-coated redoxes are smaller than those of the pristine electrode, implying that MgF_2 surface modification effectively decreases the electrode polarization. This may be possibly derived from the proper amount of MgF_2 coating layer, playing a positive role on the surfaces of the LMNO cathode active material particles, which may facilitate the Li^+ ion transfer through the interface between the LMNO particles and the electrolyte. It will be further explored and explained in the following EIS and FTIR analysis. On the other hand, two redox pairs of the 5 wt.% MgF_2-coated LMNO are shaper than those of the pristine LMNO, indicating that 5

wt.% MgF_2 surface coating effectively enhances electrode response rate.

The apparent diffusion coefficient (D_{Li}) of lithium ion can calculate from the plots (Fig. 6) in the low frequency region according to the following equations: [39,40]

$$D_{Li} = 0.5\left(\frac{RT}{AF^2\delta C_{Li}}\right)^2 \quad (1)$$

$$Zimg = K - \delta\omega^{-1/2} \quad (2)$$

where D_{Li}, lithium ion diffusion coefficient; R, the gas constant; T, the absolute temperature; F, Faraday's constant; A, the area of the electrode surface; C_{Li}, molar concentration of Li ions; ω, angular frequency region; and δ, the Warburg factor. From the plot of Zimg as a function of $\omega^{-1/2}$ (not shown), the slope δ can be obtained and D_{Li} can be calculated. The diffusivities are 1.3×10^{-10} $cm^2\ s^{-1}$ and 2.0×10^{-10} $cm^2\ s^{-1}$ for the pristine and 5 wt.% coated material, respectively, with inconspicuous change after 50 cycles. The enhancement is due to the MgF_2 coating layer prompted a shift in the phase of the material, thus effectively reducing the spatial location occupied of lithium ions by transition metals during the electrochemical reaction. This consists with the dQ/dV results in Fig. 5 and partly explains the much improved performance of LMNO after coating MgF_2 layer.

To better understand the superior cycling stability of the MgF_2-coated LMNO compared to the pristine, the impendence curves were measured after the cells at fully charged stated (4.9 V) were aged for two days to reach equilibrium. The Nyquist plots of the pristine and 5 wt.% MgF_2-coated samples at different cycles were demonstrated in Fig. 6. As widely accepted, the semicircle in high frequency region of Nyquist plot is attributed to the resistance of solid electrolyte interface (SEI) film (R_{SEI}) that covers cathode particles.[41] The second semicircle in medium frequency region is assigned to charge transfer reaction (R_{ct}), and the slope in low frequency is attributed to lithium-ion diffusion in bulk material.[42] The equivalent circuit was depicted in the inset of Fig. 6b and

parameters in Table 4 were determined by plot fitting with it. From Table 4 it can be unambiguously seen that the R_s (internal resistance of the cell), R_{SEI} and R_{ct} values of the pristine electrode is bigger than that of the 5 wt.%-coated LMNO electrode during the electrochemical cycles. This may be attributed to MgF_2 coating layer, which reduces the contact area between the electrode and electrolyte, alleviating the fast growth of interface film. Suppression of the impedance increase is favorable for elongating cell life time, which partly explains the enhanced cyclability of the modified material (Fig. 3).

Suppress of SEI growth after surface modification can also be confirmed by FTIR analysis. Fig. 7 compares the FTIR spectra of pristine and 5 wt.%-coated LMNO before and after cycling. In Fig. 7 the band at 631 cm^{-1} can be assigned to the Mn-O stretching. Two vibrations at 590 and 500 cm^{-1} can be assigned to the Ni^{2+}-O stretching mode in the structure.[43] The other four bands at 1631, 2849, 2931 and 3437 cm^{-1} are also apparent in all of the four profiles, wherein 1631 and 3437 cm^{-1} can be attributed to the ambient O-H vibrations, and 2849 and 2931 cm^{-1} can be assigned to the C-H stretching vibrations. Comparing Fig. 7a and b, no characteristic vibration corresponding to Mg-F appears after MgF_2 surface coating, which possibly derives from the low content of it in the measured sample. As can be observed in Fig. 7c and d, new absorption peaks appear after 5 cycles at the same position for pristine and the 5 wt.% MgF_2-coated LMNO besides those belonging to LMNO active material. Based on previous literatures,[44-49] detailed assignments of all the new absorption bands are listed in Table 5, which can be assigned to certain components of SEI film. Taken the above analysis into account, the SEI components of the electrodes are the same, whether MgF_2 coating layer exists. Thus, it is quite clear that the MgF_2 coating layer effectively inhibits the growth of the SEI layer, which is consistent with the EIS results in Fig. 6.

Thermal stability of electrode is of vital importance to large scale commercial applications of LIBs and the superior thermal stability of electrode will greatly contribute to desirable thermal stability of a cell. Fig. S3 (Supporting Information) compares the DSC traces of the pristine and 5 wt.% MgF_2-coated LMNO electrodes. For 5 wt.% MgF_2-coated LMNO, the exothermic peak shifts to a higher temperature of 283 ℃ compared with the 270 ℃ for the pristine LMNO. Besides, the released heat obviously decreases after 5 wt.% MgF_2 surface modification. The exothermic heat was due to the oxygen from the decomposed cathode oxide with the electrolyte.[50,51] All these results imply the improved thermal stability of MgF_2-coated LMNO electrodes.

The DSC results showed significant exothermic reaction delay and heat reduction after MgF_2 surface coating, indicating the lowered reactivity with the electrolyte. This implies that the crucial factor governing the exothermic reaction is the interfacial reaction with the electrolyte and cathode. It is also believed that the strong bonding nature of Mg-F contributes to a strong resistance to the reaction with the electrolyte, and MgF_2 has been reported to be thermally stable.[52]

Conclusions

MgF_2 nano-coated LMNO materials are successfully synthesized by a simply chemical deposition method. The electrochemical and thermal properties of LMNO electrode are greatly improved by surface modification with MgF_2 layer. Electrochemical results show that 5 wt.% MgF_2-coated LMNO presents the excellent electrochemical performances compared with pristine LMNO. It is established that the MgF_2 coating layer effectively prevents the surface of the LMNO electrode from being directly exposed to the liquid electrolyte, thereby preventing the Mn^{3+} from dissolving into the electrolyte and inhibits the fast growth of SEI layer in cycling. As a result, the

structural stability, cycling capability and thermal stability of LMNO are remarkable enhanced. Surface modification by MgF_2 is an effective way to improve the performance of LMNO cathode materials for LIBs.

ACKNOWLEDGMENT

This work was supported by the National Natural Science Foundation of China (50902044), the 863 Program of China (2015AA034201), the State Scholarship Fund from China Scholarship Council (201308410027), and the U.S. Department of Energy's Office of Basic Energy Science, Division of Materials Sciences and Engineering, under contract with UT-Battelle, LLC.

References

1 J. Lee, A. Urban, X. Li, D. Su, G. Hautier, G. Ceder, *Science*, 2014, **343**, 519–522.

2 X. Zhang, I. Belharouak, L. Li, Y. Lei, J.W. Elam, A. Nie, X. Chen, R.S. Yassar, R.L. Axelbaum, *Adv. Energy Mater.*, 2013, **3**, 1299–1307.

3 B. Dunn, H. Kamath, J.M. Tarascon, *Science*, 2011, **334**, 928–935.

4 M. Armand, J. M. Tarascon, *Nature*, 2008, **451**, 652–657.

5 X.L. Wu, Y.G. Guo, J. Su, J.W. Xiong, Y.L. Zhang, L.J. Wan, *Adv. Energy Mater.*, 2013, **3**, 1155–1160.

6 L. Zeng, C. Zheng, C. Deng, X. Ding, M. Wei, *ACS Appl. Mater. Interfaces*, 2013, **5**, 2182–2187.

7 A. Kraytsberg, Y. Ein-Eli, *Adv. Energy Mater.*, 2012, **2**, 922–939.

8 J. Xiao, X.L. Chen, P.V. Sushko, M.L. Sushko, L. Kovarik, *Adv. Mater.*, 2012, **24**, 2109–2116.

9 Y.K. Fan, J.M. Wang, Z. Tang, W.C. He, J.Q. Zhang, *Electrochim. Acta*, 2007, **52**, 3870–3875.

10 C.J. Jafta, M.K. Mathe, N. Manyala, W.D. Roos, K.I. Ozoemena, *ACS Appl. Mater. Interfaces*, 2013, **5**, 7592–7598.

11 Y. Wu, A. Manthiram, Electrochem. *Solid-State Lett.*, 2006, **9**, A221–A224.

12 J. Liu, B. Reeja-Jayan, A. Manthiram, *J. Phys. Chem. C*, 2010, **114**, 9528–9533.

13 Y.-K. Sun, Y.-S. Lee, M. Yoshio, K. Amine, *Electrochem. Solid-State Lett.*, 2002, **5**, A99–A102.

14 J. Cho, T.-J. Kim, J. Kim, M. Noh, B. Park, *J. Electrochem. Soc.*, 2004, **151**, A1899–A1904.

15 J. Cho, Y.W. Kim, B. Kim, J. Lee, B. Park, *Angew. Chem. Int. Ed.*, 2003, **115**, 1618–1621.

16 Y. Bai, Q.J. Chang, Q. Yu, S. Zhao, K. Jiang, *Electrochim. Acta*, 2013, **112**, 414–421

17 Y. Bai, Y.F. Yin, N. Liu, B.K. Guo, H.J. Shi, J.Y. Liu, *J. Power Sources*, 2007, **174**, 328–334.

18 S.T. Myung, K. Izumi, S. Komaba, *Chem. Mater.*, 2005, **17**, 3695–3704.

19 J.Y. Liu, N. Liu, D.T. Liu, Y. Bai, L.H. Shi, Z.X. Wang, L.Q. Chen, V. Hennige, A. Schuch, *J. Electrochem. Soc.*, 2007, **154**, A55–A63.

20 Myung S, Izumi K, Komaba S, Sun Y, Yashiro H, Kumagai N, *Chem. Mater.*, 2005, **17**, 3695–3704.

21 Myung S, Izumi K, Komaba S, Yashiro H, Bang HJ, Sun Y, Kumagai N, *J. Phys. Chem. C*, 2007, **111**, 4061–4067.

22 Y. Bai, K. Jiang, S.W. Sun, Q. Wu, X. Lu, N. Wan, *Electrochim. Acta*, 2014, **134**, 347–354.

23 Y. Cho, J. Eom, J. Cho, *J. Electrochem. Soc.*, 2010, **157**, A617–A624.

24 H.J. Lee, S.B. Kim, Y.J. Park, *Nanoscale Res. Lett.*, 2012, **4**, 137–143.

25 H.J. Lee, Y.J. Park, *Solid State Ionics*, 2013, **230**, 86–91.

26 H. Duncan, Y. Abu-Lebdeh, I.J. Davidson, *J. Electrochem. Soc.*, 2010, **157**, A528–A535.

27 M. Kunduraci, G.G. Amatucci, *J. Electrochem. Soc.*, 2006, **153**, A1345–A1352.

28 Y. Ein-Eli, B. Markovsky, D. Aurbach, Y. Carmeli, H. Yamin, S. Luski, *Electrochim. Acta*, 1994, **39**, 2559–2569.

29 Charl J. Jafta, Mkhulu K. Mathe, Ncholu Manyala, Wiets D. Roos, Kenneth I. Ozoemena, *ACS Appl. Mater. Interfaces*, 2013, **5**, 7592–7598.

30 L.P. Wang, H. Li, X.J. Huang, E. Baudrin, *Solid State Ionics*, 2011, **193**, 32–38.

31 J.S. Chae, S.B. Yoon, W.S. Yoon, S.M. Park, *J. Alloy. Compd.*, 2014, **601**, 217–222.

32 L.Mao, L.Shen, J.H. Chen, Y.Wu, Minsuk Kwak, Y. Lu, Q.Xue, J. Pei, L.Zhang, G.Y. Yuan, R.Fan, J.B. Ge, W.J. Ding, *ACS Appl. Mater. Interfaces*, 2015, **7**, 5320−5330.

33 J. F. Moulder, W. F. Stickle, P. E. Sobol, K. D. Bomben, Handbook of X-ray Photoelectron Spectroscopy; Perkin Elmer: Eden Prairie, MN, 1992; Vol. 40.

34 H.J. Lin, Junko Matsuda, H.W. Li, M. Zhu, Etsuo Akiba, *Journal of Alloys and Compounds*, doi:10.1016/j.jallcom.2014.12.102.

35 B. Kang, S.T. Myung, K. Amine, S.M. Lee, Y.K. Sun, *J. Power Sources*, 2010, **195**, 2023–2028.

36 G.Q. Liu, L. Wen, X. Wang, B.Y. Ma, *J. Alloy. Compd.*, 2011, **509**, 9377–9381.

37 N.M. Hagh, G.G. Amatucci, *J. Power Sources*, 2010, **195**, 5005–5012.

38 L. Maugeri, L. Simonelli, A. Ladecola, B. Joseph, M. Okubo, I. Honma, H. Wadati, T. Mizokawa, N.l. Saini, *J. Power Sources*, 2013, **229**, 272–276.

39 F. Wu, Z. wang, X. Li, L.Wu, X. Wang, X. Zhang, Z. wang, X. Xiong, H. Guo, *J. Alloys*

Compd., 2011, **509**, 596–601.

40 J.F. Ni, H.H. Zhou, J.T. Chen, X.X. Zhang, *Electrochim. Acta*, 2008, **53**, 3075–3083.

41 T. Hutzenlaub, S. Thiele, R. Zengerle, C. Ziegler, Electrochem. *Solid-State Lett.*, 2012, **15**, A33–A36.

42 J. Liu, A. Manthiram, *J. Phys. Chem. C*, 2009, **113**, 15073–15079.

43 J.S. Chae, S.B. Yoon, W.S. Yoon, S.M. Park, *J. Alloy. Compd.*, 2014, **601**, 217–222.

44 D. Aurbach, B. Markovsky, A. Shechter, Y. Ein-Eli, H. Cohen, *J. Electrochem. Soc.*, 1996, **143**, 3809–3820.

45 K.I. Morigaki, A. Ohta, *J. Power Sources*, 1998, **76**, 159–166.

46 D. Aurbach, Y. Gofer, M. Benzion, P. Aped, *J. Electroanal. Chem.*, 1992, **451**, 339–342.

47 H. Duncan，D. Duguay, Y. Abu-Lebdeh, I.J. Davidson, *J. Electrochem. Soc.*, 2011, **158**, A537–A550.

48 D. Aurbach, M.D. Levi, E. Levi, A. Schechter, *J. Phys. Chem. B*, 1997, **101**, 2195–2198.

49 D. Aurbach, J. Power Sources, 2000, **89**, 206–218.

50 M.H. Liu, H.T. Huang, C.M. Lin, J.M. Chen, S.C. Liao, *Electrochim. Acta*, 2014, **120**, 133–139.

51 Meike Fleischhammer, Peter Axmann, Gunther Bisle, Roberto Marassi, Margret Wohlfahrt-Mehrens, *ILED, Rome*, 2014, **5**, 28–30.

52 X.W. Sun, T. Song, X.P. Wei, W.L. Quan, X.B. Liu, W.F. Su, *Mater. Res. Bull.*, 2014, **52**, 151–157.

Table 1. Lattice parameters and Grain size of LMNO before and after MgF_2 surface modification obtained from the XRD patterns.

Sample	Pristine	3 wt.%-coated	5 wt.%-coated	7 wt.%-coated
Lattice parameter (Å)	8.1698	8.1611	8.1614	8.1612
Grain size (nm)	54.5	54.3	54.4	54.3

Table 2. Cycling performance of pristine and 5 wt.% MgF_2-coated LMNO.

Sample	Initial discharge Capacity (mAh g^{-1})	50^{th} discharge Capacity (mAh g^{-1})	Retention Rate (%)	100^{th} discharge Capacity (mAhg^{-1})	Retention Rate (%)
Pristine	121.4	98.7	81.3	84.1	69.3
3 wt.%-coated	116.8	96.2	82.3	85.0	72.8
5 wt.%-coated	115.3	112.2	97.3	103.7	89.9
7 wt.%-coated	109.6	85.2	77.7	70.4	64.2

Table 3. Redox potentials and D-Values of pristine and MgF_2-coated LMNO.

Redox potential (V)		D-Value(V) [a]	
Pristine	5 wt.% MgF_2	pristine	5 wt.% MgF_2
4.04/3.97	4.03/4.00	0.07	0.03
4.70/4.64	4.69/4.67	0.06	0.02
4.76/4.70	4.75/4.72	0.06	0.03

[a] The difference between redox pairs.

Table 4. EIS data of pristine and 5 wt.% MgF_2-coated LMNO electrodes.

Sample	Resistance	0^{st}	10^{th}	20^{th}	50^{th}	80^{th}	100^{th}
pristine	R_s	3.1	3.6	4.0	4.2	4.3	4.7
	R_{sf}	1560.0	303.3	499.0	573.8	735.5	985.7
	R_{ct}	390.2	478.6	560.6	629.3	681.7	832.2
5 wt.% MgF_2-coated	R_s	2.9	3.2	3.3	3.5	3.7	3.8
	R_{sf}	1384	289.5	318.8	378.6	436.7	474.7
	R_{ct}	232.7	253.0	269.6	278.1	289.4	315.7

Table 5. New infrared peaks and the corresponding assignments.

Peak position	Assignment
862	Li_2CO_3 C-O st [44,45]
1074	Li_2CO_3 C-O st [44,46]
1116	$ROCO_2Li$ CO_3^{2-} bend [45]
1187	$Li_xPF_yO_z$ [47]
1262	CH_2OCO_2Li [44]
1471	Li_2CO_3 C-O st [45,48]
1776	Carbonyl (C=O) stretch of SEI [49]

Figure Captions

Fig. 1. XRD patterns of the pristine and MgF_2-coated LMNO samples.

Fig. 2. Surface morphologies of pristine (a) 3 wt.% (b) 5 wt.% (c) and 7 wt.% (d) MgF_2-coated LMNO and EDS mapping of F (e) and Mg (f) for 5 wt.% MgF_2-coated LMNO. TEM images of (g) pristine and (h) 5 wt.% MgF_2-coated LMNO.

Fig. 3. Cycling performance of pristine and MgF_2-coated LMNO.

Fig. 4. The charge-discharge curves of pristine and MgF_2-coated LMNO.

Fig. 5. dQ/dV vs. voltage curves of the pristine and 5 wt.% MgF_2-coated LMNO.

Fig. 6. Nyquist plots of the pristine (a) and 5 wt.%-coated LMNO (b) after different cycles.

Fig. 7. FTIR spectra of the pristine and 5 wt.%-coated LMNO.

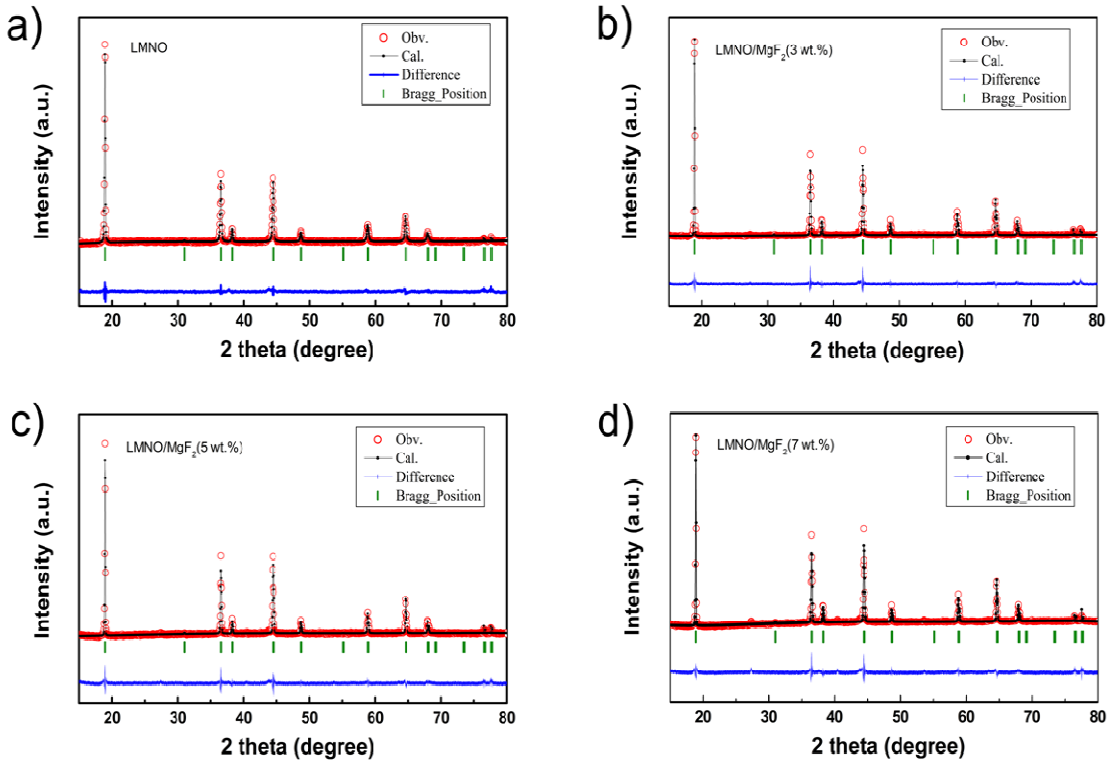

Fig. 1. XRD patterns of the pristine and MgF_2-coated LMNO samples.

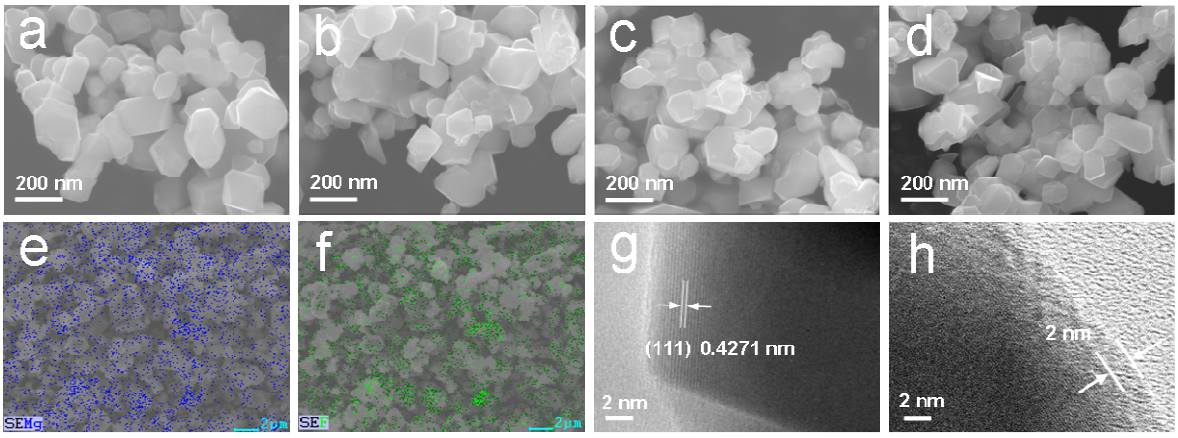

Fig. 2. Surface morphologies of pristine (a) 3 wt.% (b) 5 wt.% (c) and 7 wt.% (d) MgF_2-coated LMNO and EDS mapping of F (e) and Mg (f) for 5 wt.% MgF_2-coated LMNO. TEM images of (g) pristine and (h) 5 wt.% MgF_2-coated LMNO.

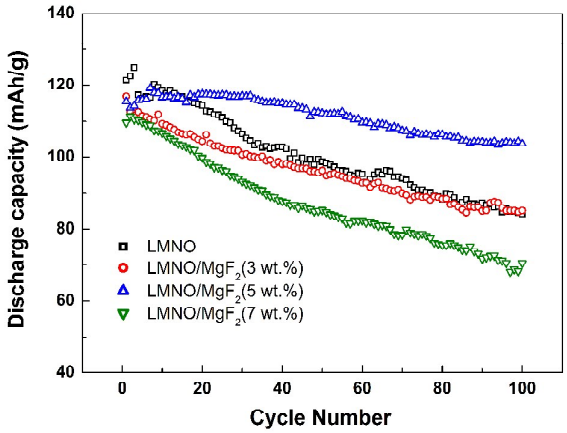

Fig. 3. Cycling performance of pristine and MgF_2-coated LMNO.

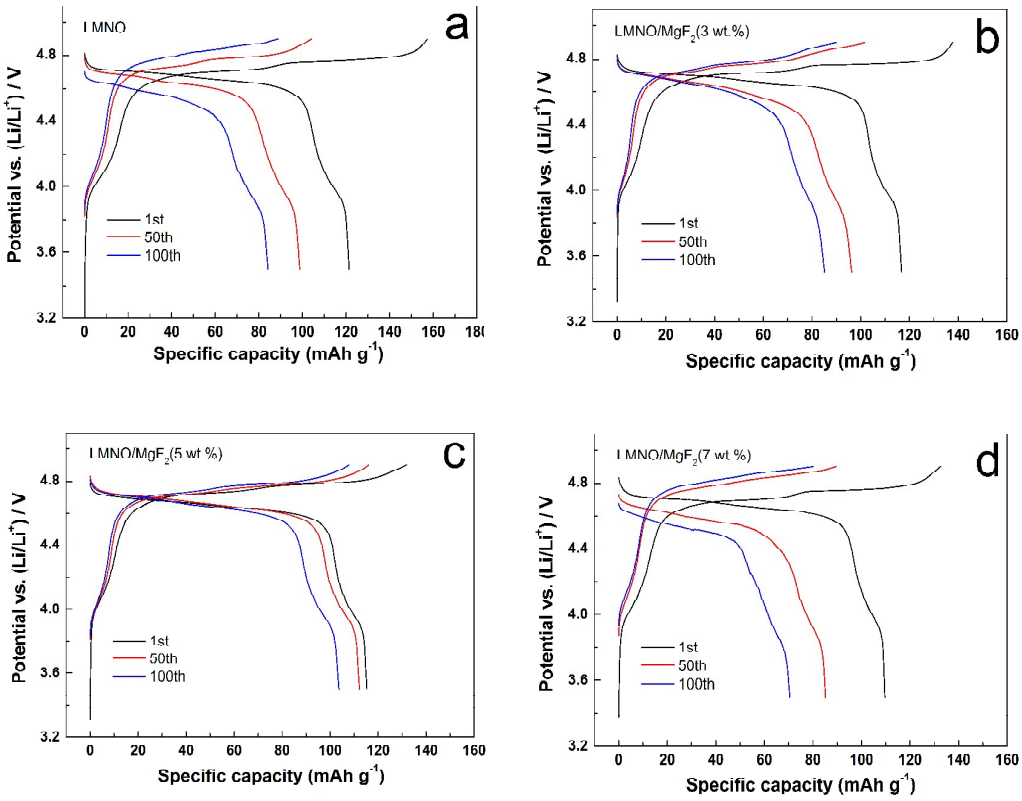

Fig. 4. The charge-discharge curves of pristine and MgF_2-coated LMNO.

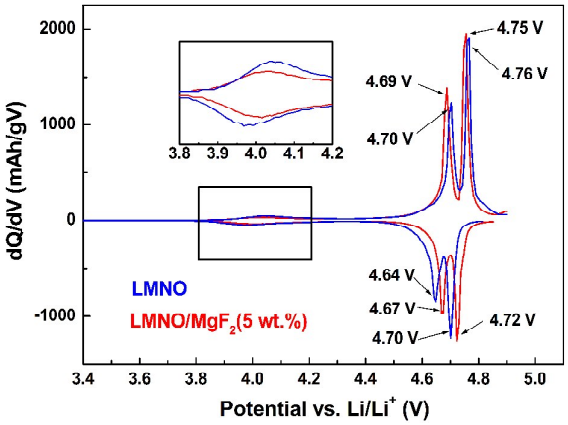

Fig. 5. dQ/dV vs. voltage curves of the pristine and 5 wt.% MgF_2-coated LMNO.

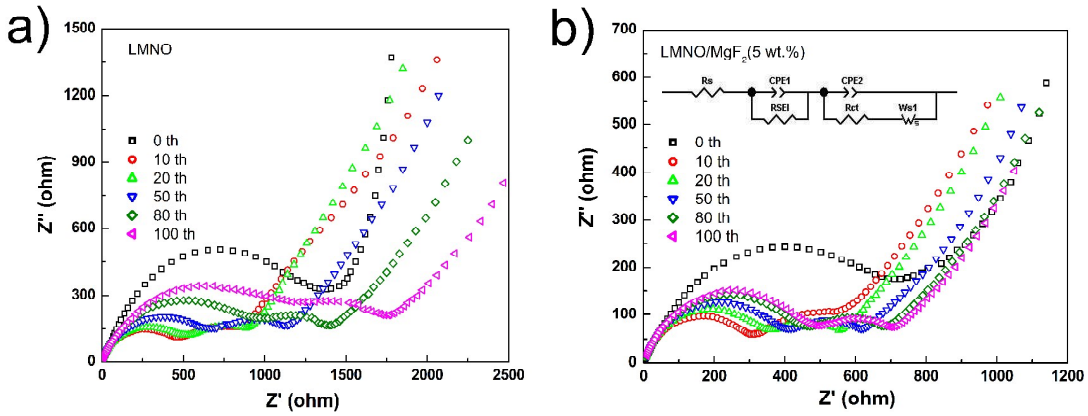

Fig. 6. Nyquist plots of the pristine (a) and 5 wt.%-coated LMNO (b) after different cycles.

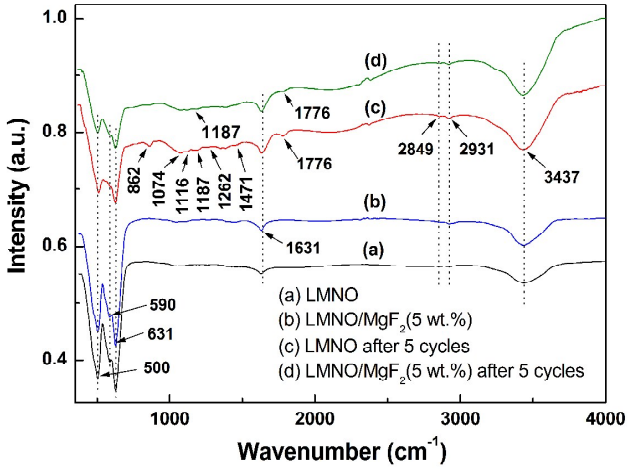

Fig. 7. FTIR spectra of the pristine and 5 wt.%-coated LMNO.